Cristina Trillo, Ángel F. Doval, J. Luis Deán and Socorro Hernández-Montes, "Numerical reconstruction of acoustic bulk waves in aluminium from TV holography surface displacement measurements," Proc. SPIE 7098, "Eighth International Conference on Vibration Measurements by Laser Techniques: Advances and Applications", 70980G (June 17, 2008)

http://dx.doi.org/10.1117/12.802984

Numerical reconstruction of acoustic bulk waves in aluminium from TV holography surface displacement measurements

Cristina Trillo[a,*], Ángel F. Doval[a], J. Luis Deán [a] and Socorro Hernández-Montes[b]

[a]Universidade de Vigo. Departamento de Física Aplicada. E.T.S. de Ingenieros Industriales. Campus de Lagoas-Marcosende. E36310 Vigo, Spain.
[b]Centro de Investigaciones en Óptica, A.C. Loma del Bosque 115. C.P. 37150 León, Gto. (México)

ABSTRACT

The paper describes a hybrid technique, aimed at nondestructive inspection of materials, that combines whole-field optic measurements, acoustic excitation and a numerical reconstruction method. The interior of a thick specimen is probed by short bursts of narrowband ultrasonic bulk waves. The acoustic wavefronts that constitute the burst emerge at the opposite face of the sample and induce periodic displacements of its surface. These displacements are measured by TV holography, a whole-field optical technique, also known as electronic speckle pattern interferometry (ESPI). The measurement process yields the complex amplitude (i.e., amplitude and phase) of the acoustic wavefronts at the plane of the surface as a series of 2-D, complex-valued maps. Lastly, a numerical reconstruction algorithm that uses the Rayleigh-Sommerfeld diffraction formula is employed to calculate the amplitude and phase of the acoustic wavefronts at any other plane in the interior of the specimen. This procedure is analogous to the numerical reconstruction of optical object wavefronts in digital holography (with light and free space taking the place of acoustic waves and the material medium, respectively), so the present method could also be designated as digital opto-acoustic holography. If the wavefronts are affected by the presence of inhomogeneities in the medium, information about the shape and position of such defects could be retrieved from the reconstructed wavefront at the appropriate depth. The technique herein proposed was successfully tested in an alluminium specimen with an artificial defect.

Keywords: ESPI, TV holography, Digital Opto-acoustic Holography, acoustic waves, numerical reconstruction

1. INTRODUCTION

The technique presented in this paper, a combination of whole-field optical measurements, acoustic excitation and numerical reconstruction methods, is aimed at nondestructive testing of materials. The underlying principle is not new: if the amplitude and phase of a wavefront are known at a given plane, then the wavefront can be reconstructed at other planes. The reconstruction can be optical, as is the case of light waves in classical holography, or numerical, as it is usual in acoustic holography. The numerical reconstruction of light waves is also possible and is commonly known as digital holography.

In this work, we focus our attention in ultrasonic bulk waves that propagate in solids. Since the ultrasonic waves probe the interior of the specimen, the wavefronts that arrive at the surface carry information about the traversed material, and the presence of defects and another features could then be detected and their position located inside the specimen. The distinctive feature of the herein proposed technique is the way in which the amplitude and phase information of the acoustic wavefield are recorded. The measurement is performed without need for an acoustic reference wave. The measurement plane is on the surface of the specimen, where the waves emerge after traversing the sample. The complex amplitude is obtained from the displacements that these wavefronts induce at the surface. These displacements are measured with a non contact, whole-field optical technique, namely TV holography, also known as electronic speckle pattern interferometry (ESPI). Both the mechanical amplitude and phase of the wavefield are recorded, and the measurement is performed simultaneously at all the points of the field of view. Since the acoustic wave is completely characterized at one

*C.T.Y.: E-mail: mctrillo@uvigo.es

Eighth International Conference on Vibration Measurements by Laser Techniques: Advances and Applications, edited by Enrico Primo Tomasini, Proc. of SPIE Vol. 7098, 70980G, (2008) 0277-786X/08/$18 doi: 10.1117/12.802984

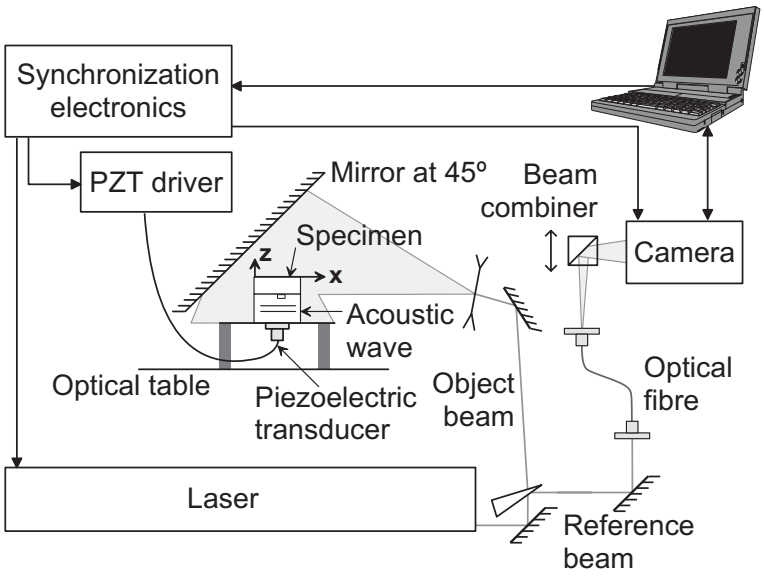

Figure 1. Experimental setup.

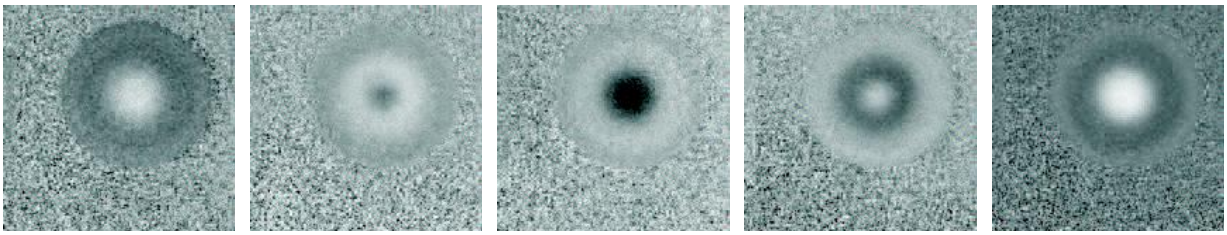

Figure 2. Sequence of optical phase-change maps recorded at intervals of one quarter of the oscillation period of the wave (T_{M}). The periodic displacement experienced by the surface of the specimen is clearly seen.

plane (the surface of the specimen in our case) it can be numerically propagated towards the interior of the sample. If the wavefronts have been diffracted by defects in the material, a backpropagation would be able to locate the source of the perturbation, i.e., the defect, when the reconstruction is calculated at the appropriate depth.

The optical technique that measures the mechanical complex amplitude of the acoustic field is briefly described in section 2.1. The details are reported in reference 2, but a summary of the main points was considered of interest for the sake of self-containment. In section 2.2 the numerical reconstruction procedure applied to the measured acoustic field is described. Sections 3 and 4 contain respectively the experimental details and some results obtained in an aluminium test specimen with an artificial flaw.

2. THEORY

2.1 Full-field measurement of the amplitude and phase of acoustic wavefronts

Figure 1 shows the setup used in our experiments. A short burst of acoustic waves that propagates through a sample induces a displacement of the observed surface as the constituent wavefronts emerge. This surface is illuminated with four laser pulses coming from a twin-cavity, frequency doubled, Nd:YAG laser. The illumination geometry makes the interferometer sensitive to the out-of-plane component of the displacement.

Two deformed states of the surface are recorded in two pairs of primary correlograms taken with a CCD camera and processed with the spatial Fourier transform method.[1] The result is a 2-D optical phase-change map

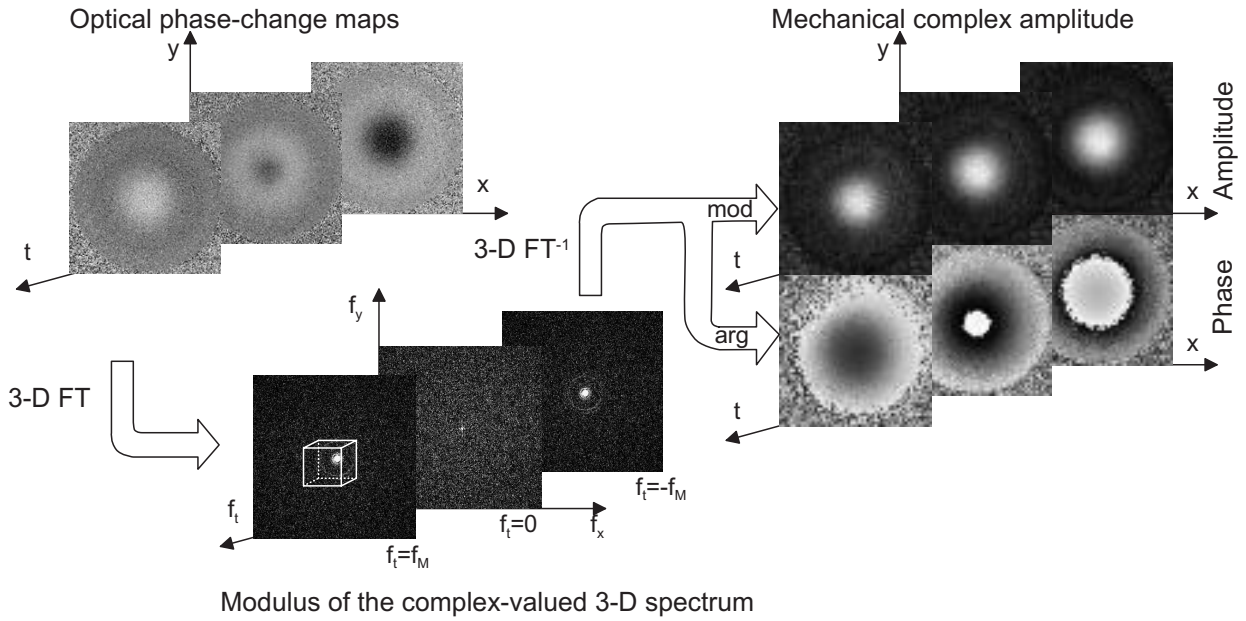

Figure 3. Sketch of the 3-D Fourier transform processing applied to the measured data.

that encodes the displacement of the surface at a given instant t_1. Then, the synchronization system increases the time interval between the excitation of the burst and the acquisition of the correlograms, and a new optical-phase change map at an instant t_2 is obtained. This process is repeated N times. The displacement of the surface induced by the arrival of successive wavefronts can be thus registered in a sequence of N optical phase-change maps (see Figure 2).

To obtain the complex amplitude of the wavefronts, the image processing sketched in Figure 3 is applied to the data set.[2] Firstly, a 3-D spatiotemporal (2-D spatial, 1-D temporal) Fourier transform of the N optical phase-change maps is performed. Then, a 3-D bandpass filter is applied to retrieve the wave's spectral content. Lastly, a 3-D inverse Fourier transform yields N complex-valued maps that encode the mechanical amplitude and phase of the acoustic wavefronts.

It was observed that, shortly after the arrival of the first bulk wavefronts, an additional set of waves that propagate on the surface appears. One option to prevent them from hindering the reconstruction process of the bulk wavefronts is to tailor the 3-D filter in Figure 3 to remove their spectral content. A simpler alternative is used in this paper: only the complex-valued maps corresponding to the first-arriving wavefronts are considered for the reconstruction process.

2.2 Numerical backpropagation of acoustic wavefronts

In the reference system we have selected (see Figures 1 or 5) a burst of acoustic waves propagates along the positive direction of the z axis. Assuming that the acoustic wavefronts are plane, the instantaneous out-of-plane acoustic displacement $U(x, y, z, t)$ at the surface of the sample can then be written as

$$U\left(x, y, z, t\right) = A_{\mathrm{M}}(x, y, z, t)\,\mathrm{Re}\left[\exp\left[j\left(\varphi_{\mathrm{M}} + k_{\mathrm{M}} z - \omega_{\mathrm{M}} t\right)\right]\right] \tag{1}$$

where A_{M} is the amplitude of the wave; φ_{M} is the initial phase; $k_{\mathrm{M}} = 2\pi/\lambda_{\mathrm{M}}$ is the wavenumber; λ_{M} is the wavelenght; $\omega_{\mathrm{M}} = 2\pi/T_{\mathrm{M}}$ is the angular frequency; $T_{\mathrm{M}} = 1/f_{\mathrm{M}}$ is the period of the wave and f_{M} is its temporal frequency.

Provided that the amplitude and phase of a wavefront are known on a given plane at position $z_0 = 0$, the amplitude and phase at any other position z can be calculated by means of the Rayleigh-Sommerfeld diffraction

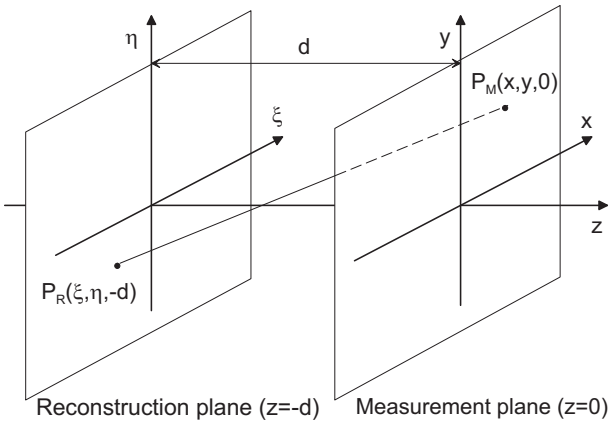

Figure 4. Geometry used to describe the reconstruction process.

formula, which, in cartesian coordinates, has the form[3]

$$U(\xi,\eta,z,t)=\iint_{-\infty}^{\infty}U(x,y,z_0,t)\frac{1}{j\lambda_{\mathrm{M}}}\frac{\exp\left(jk_{\mathrm{M}}z\sqrt{1+\left(\frac{\xi-x}{z}\right)^2+\left(\frac{\eta-y}{z}\right)^2}\right)}{z\left[1+\left(\frac{\xi-x}{z}\right)^2+\left(\frac{\eta-y}{z}\right)^2\right]}dxdy \tag{2}$$

Figure 4 shows the geometry used to describe the numerical reconstruction process. The measurement plane is located, in our case, on the surface of the sample, where we measure the actual mechanical amplitude and phase of the arriving wavefronts. The reconstruction plane is located in the interior of the material that the wave has traversed, i. e. $z<0$.

Equation (2) can be interpreted as the convolution of the measured field $U(x,y,z_0,t)$ with an impulse response given by

$$h\left(x,y\right)=\frac{\exp\left(jk_{\mathrm{M}}z\sqrt{1+\left(\frac{\xi-x}{z}\right)^2+\left(\frac{\eta-y}{z}\right)^2}\right)}{j\lambda_{\mathrm{M}}z\left[1+\left(\frac{\xi-x}{z}\right)^2+\left(\frac{\eta-y}{z}\right)^2\right]} \tag{3}$$

and, according to the convolution theorem, the field $U(\xi,\eta,z,t)$ can be calculated as a sequence of direct and inverse Fourier transformations

$$U(\xi,\eta,z,t)=U(x,y,z_0,t)*h\left(x,y\right)=\mathcal{F}^{-1}\left\{\mathcal{F}\left[U(x,y,z_0,t)\right]\mathcal{F}\left[h\left(x,y\right)\right]\right\} \tag{4}$$

In this equation, $*$ denotes the convolution operation, and $\mathcal{F}$ the Fourier transform, which can be efficiently computed by means of the fast Fourier transform (FFT) algorithm.

The numerical expression of the analytical impulse response in Equation (3) can be written as[3,4]

$$h\left(k,l\right)=\frac{\exp\left(jk_{\mathrm{M}}z\sqrt{1+\frac{[k-(N_y/2)]^2\Delta x^2}{z^2}+\frac{[l-(N_x/2)]^2\Delta y^2}{z^2}}\right)}{j\lambda_{\mathrm{M}}z\left(1+\frac{[k-(N_y/2)]^2\Delta x^2}{z^2}+\frac{[l-(N_x/2)]^2\Delta y^2}{z^2}\right)},\ \text{with } k=1,\ldots N_y; l=1,\ldots N_x \tag{5}$$

Δx and Δy denote the length of the sampling step in the measurement plane along the x and y coordinate axes respectively. N_x and N_y are the length of the sampling array along the same axes.

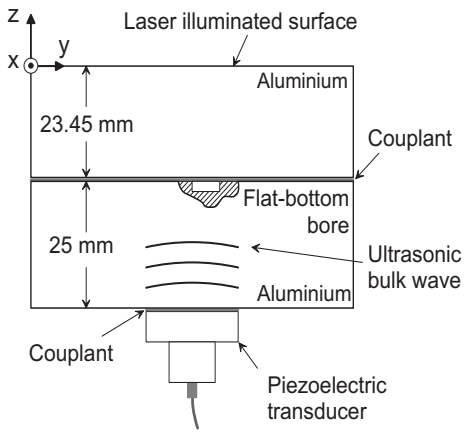

Figure 5. Geometry of the specimen used in the experiments. The couplants are thin films of glycerine and honey of negligible thickness. The flat bottomed bore drilled in the lower block is 1 mm deep and has a diameter of 6 mm.

3. EXPERIMENTAL

The light source is a Spectron Nd:YAG pulsed laser which works at a repetition rate of 25 Hz. It comprises two independent cavities and a common injection seeder. The infrared output is doubled to 532 nm. The pulses are separated by 1.5 μs, and their duration is ~ 20 ns.

For our tests we used an specimen made of two aluminium cylinders of the same diametre (70 mm) The upper block is 23.45 mm thick and was chemically treated to have a matt finish. The lower block is 25 mm thick. A 6 mm diametre, 1 mm deep flat-bottomed bore was drilled near the centre of the coupling face of the lower block (see Figure 5) to simulate a hidden flaw in the sample. To build the specimen, a few drops of glycerine are deposited on the flawed face, and both cylinders are coupled together by a combination of gentle pressure and shear.

The generation system consists of a resonant piezoelectric transducer and its corresponding driver. The transducer is coupled with honey to the lower block. The driver produces high-voltage tone-bursts, and permits the selection of both the number of cycles and the central frequency in the range of a few MHz. In our experiments, the driving frequency is 1 MHz and the number of pulses per burst is set to 5. Every time the driver is triggered by the synchronization system, the sample is insonified with a burst of narrowband bulk waves. The longitudinal velocity (c_{L}) of bulk waves in aluminium is about 6330 $\mathrm{m\,s^{-1}}$; therefore, the expected wavelength is $\lambda_{\mathrm{M}} \approx 6.33$ mm.

The necessary data collection is carried out in 64 experiments, conducted as indicated in section 2.1, and the same number of optical-phase change maps is obtained. The correlograms of each pair are recorded within an interval of 1.5 μs in a thermo-cooled double-exposure CCD camera (PCO *Double-Shutter*) with a sensor size of 1280×1024 pixels. However, the FFT algorithm used throughout imposes that the data size in any dimension must be an integer power of 2, so the size of the resultant optical phase-change maps is reduced to 1024×1024 pixels.

The time interval between the excitation of the wave burst and the acquisition of the correlograms is increased in steps of $T_{\mathrm{M}}/4 = 250$ ns from one experiment to the next. Thus, every wavefront is recorded at four instants of its oscillation period, which is enough to comply with the sampling theorem. The initial time interval is selected so that the first-arriving wavefronts are located just below the surface in the first images*. The output of the subsequent 3-D processing stage (see Figure 3 and section 2.1) is thus a set of 64 complex-valued maps which encode the mechanical amplitude and phase of the wavefronts that arrive to the observed surface at the recording instants. We selected the thirteenth complex map of the sequence to test the numerical backpropagation algorithm.

*Note that the optical phase-change maps shown in Fig. 2 are actually the items 8 to 12 of a sequence, so the surface displacement can already be detected in the first image.

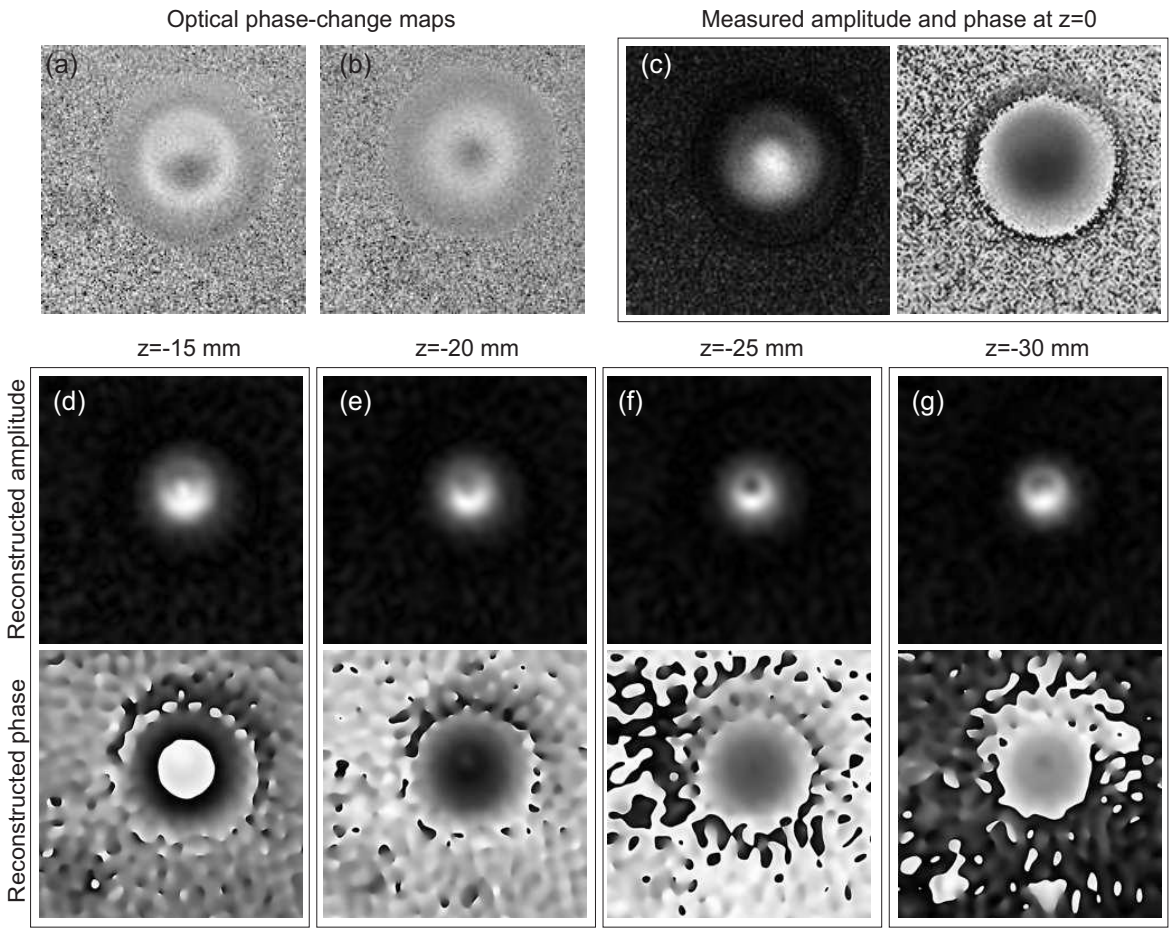

Figure 6. (a) Optical phase-change map of the excited test specimen shown in Figure 5 at a given instant t_1. (b) Optical phase-change map of an excited flawless specimen at the same instant. (c) Measured mechanical amplitude and phase of the wavefront that reaches the surface at t_1 (d)-(g) The wavefront measured in (c) is reconstructed at the indicated distances.

The values taken by N_x and N_y in the reconstruction process are $N_x = N_y = 1024$. The sampling steps Δx and Δy are calculated as the area, measured on the surface of the sample, that is covered by one pixel. For that purpose, an image of the specimen in white light was taken. The diametre measured in the image yielded a result of 646 pixels for the actual length of 70 mm. Since the sensor has square pixels, $\Delta x = \Delta y = 70$ mm /646 pixel = 0.11 mm pixel^{-1}. The only variable in the reconstruction algorithm is the reconstruction distance z, which must be $z < 0$ to backpropagate the measured field towards the interior of the sample.

4. RESULTS

Figure 6(c) shows the mechanical amplitude and phase of the map that was selected to test the numerical reconstruction process. The surface displacement pattern due to the wave is more clearly seen in the corresponding optical phase-change map shown in 6(a). Figure 6(b) shows the result obtained when the same experimental procedure as described in the previous section is carried out on a flawless specimen, and is included here just for comparison purposes. Note the difference between the symmetric pattern in 6(b) and the asymmetry that arises in 6(a) due to the effect of the flaw. Both images 6(a) and 6(b) were digitally processed to enhance the contrast.

Several values of z were tested, ranging from -10 mm to -30 mm in steps of 1 mm. The obtained results for $z = -15, -20, -25$ and -30 mm are shown in Figures 6(d) to 6(g). The presence of the defect is apparent in the maps of reconstructed mechanical amplitude as a black speck in the wavefront. The blurred outline of

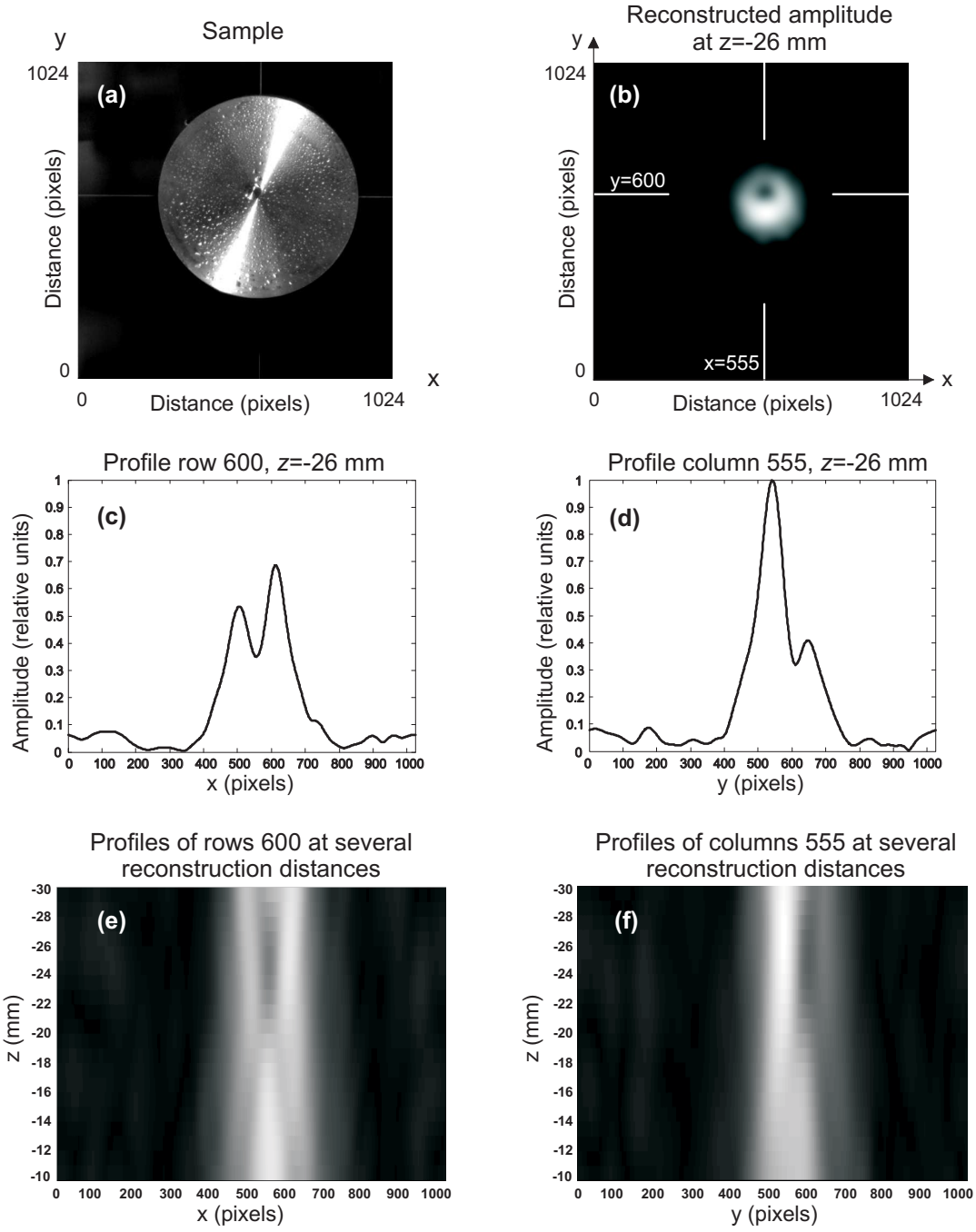

Figure 7. (a) Image of the lower cylinder of the test specimen. The size and position of the bore can be clearly seen. The bright specks are due to the glycerine (used as a couplant between the blocks) which coalesced into small drops after the upper block was removed to take the picture. (b) Reconstructed amplitude at a distance $z = -26$ mm. (c) Amplitude profile along the coordinate $y = 600$. (d) Amplitude profile along the coordinate $x = 555$. (e) 2-D view of the amplitude profiles along the coordinate $y = 600$ taken for different reconstruction distances. (f) 2-D view of the amplitude profiles along the coordinate $x = 555$. The amplitudes in (c) and (d) are represented as grey levels in (d) and (f). Black and white correspond to amplitude values of 0 and 1, respectively.

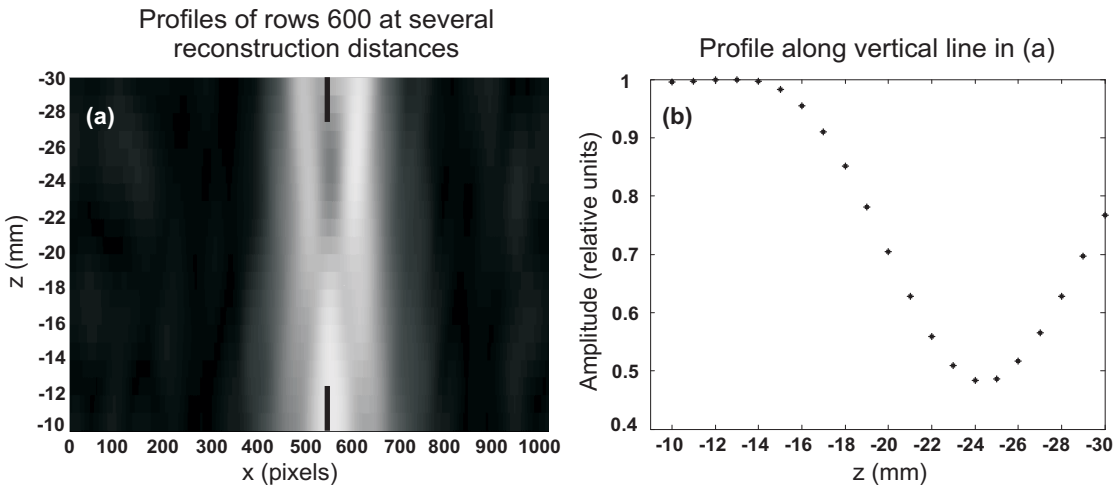

Figure 8. (a) 2-D view of the amplitude profiles along the coordinate $x = 555$ in Figure 7(b). (b) Intensity profile along the column indicated by two vertical black lines in (a). The minimum is reached for a value of the reconstruction distance that coincides with the position of the defect in the specimen.

the spot is brought to the best focus for the map reconstructed at $z = -25$ mm, which is in agreement with the actual depth of the defect (see Figures 5 and 8).

The reconstructed mechanical amplitude at position $z = -26$ mm is presented in Figure 7(b). For comparison purposes, a white light picture of the lower block of the sample is shown in 7(a). We observe that the size and position of the defect are also quite in agreement with the size and position of the shadow in the mechanical amplitude map. The presence of the defect is also apparent in Figures 7(c) and 7(d), which show the intensity profiles plotted along the horizontal and vertical lines, respectively, marked in figure 7(b). Finally, we take the reconstructed mechanical amplitude maps obtained for different values of z and extract the profiles along the coordinates indicated in 7(b). These horizontal and vertical profiles are represented against the reconstruction distance in Figures 7(e) and 7(f) respectively. The local drop in the intensity profile observed in Figures 7(c) and 7(d) appears here as a dark shadow against the bright background in the range of distances from $z = -20$ to $z = -30$ mm. The drop is more pronounced in the darkest region at the centre of this interval, in the vicinity of $z \approx -25$ mm. However, the edges of this region are too blurry to determine where the sharpest drop is located. It is useful, then, to inspect the intensity profile along one of the columns in Figures 7(e) or 7(f). We chose the column at position $x = 600$ pixels in Figure 7(e). Its position is indicated by means of two vertical black lines in Figure 8(a). The amplitude profile along this line is shown in 8(b). Now it is clear that the sharpest drop in intensity takes place between $z = -24$ and $z = -25$ mm. This result is in good agreement with the actual position of the bottom of the bore, located at $z = -(23.45 \text{ mm} + 1 \text{ mm}) = -24.45$ mm (see Figure 5).

5. CONCLUSIONS

We present a hybrid opto-acoustic technique aimed at the nondestructive inspection of materials. The proposed technique, which could be designed as Digital Opto-acoustic Holography, combines optical, acoustic and numerical methods as follows:

- Acoustic excitation. An specimen is insonified with short bursts of narrowband ultrasonic waves. The waves traverse the material and eventually emerge at the opposite surface.
- Optical measurement. The displacement experienced by the surface of the specimen due to the arrival of the acoustic waves is measured by means of a TV-holography technique. The output is a series of complex-valued 2-D maps that contain both the amplitude and phase of the acoustic wavefronts at the plane of the surface.

- Numerical propagation of wavefronts. The mechanical amplitude and phase of the acoustic wave can be numerically reconstructed at any plane between the acoustic source and the opposite surface of the specimen by applying a numerical implementation of the Rayleigh-Sommerfeld diffraction formula.

This hybrid technique was tested in an aluminium specimen with an artificial defect, and showed promising results in the detection and localization of flaws.

ACKNOWLEDGMENTS

This work was co-funded by the Spanish *Ministerio de Educación y Ciencia* and by the European Comission (ERDF) in the context of the *Plan Nacional de I+D+i* (project number DPI2005-09203-C03-01) and by the *Dirección Xeral de Investigación, Desenvolvemento e Innovación da Xunta de Galicia* in the context of the *Plan Galego de IDIT* (project number PGIDIT06PXIC303193PN). Supplementary co-funding from the *Universidade de Vigo* (project number I608122F64102) is also acknowledged.

REFERENCES

[1] C. Trillo, Á. F. Doval and M. Pérez-Amor, "Enhanced measurement of ultrasonic surface acoustic waves with TV holography by correction of phase mismatch between laser cavities," in *Speckle06: Speckles, from grains to flowers*, P. Slangen, C. Cerruti, eds., Proc. SPIE □**341**, pp. 63412X-1 to 63412X-1, 2006

[2] C. Trillo and Á. F. Doval, "Spatiotemporal Fourier transform method for the measurement of narrowband ultrasonic surface acoustic waves with TV holography," in *Speckle06: Speckles, from grains to flowers*, P. Slangen, C. Cerruti, eds., Proc. SPIE □**341**, pp. 63410M-1 to 63410M-6, 2006.

[3] J. D. Gaskill, *Linear systems, Fourier transforms and Optics*, John Wiley & Sons, 1978.

[4] U. Schnars and W. Jueptner, *Digital Holography*, chapter 3, Springer-Verlag, Berlin, Heidelberg, 2005.